Ultrahigh Capacitive Supercapacitor Derived from Self-Oxygen Doped Biomass-Based 3D Porous Carbon Sources

by Rika Taslim

Submission date: 13-Apr-2023 02:30PM (UTC+0700)
Submission ID: 2063299689
File name: 14._Daun_pisang_chemnanomat22.pdf (1.62M)
Word count: 9038
Character count: 46966

ACES Asian Chemical Editorial Society

doi.org/10.1002/cnma.202100388

CHEMNANOMAT
Full Paper

www.chemnanomat.org

Ultrahigh Capacitive Supercapacitor Derived from Self-Oxygen Doped Biomass-Based 3D Porous Carbon Sources

E. Taer,*[a] R. Taslim,[b] and A. Apriwandi[a]

Abstract: This study reported an ultrahigh specific capacitance of a supercapacitor, using self-oxygen doped 3D-porous carbon derivatives from dried banana leaves. The samples were synthesized by $ZnCl_2$ impregnation at different temperature pyrolysis of 700–900 °C. Furthermore, the overall process significantly increased the specific surface area from 429.6 to 860.4 $m^2 g^{-1}$ followed by the formation of 3D-interconnected pores structures. Unexpectedly, the activated carbon demonstrated high-level oxygen dopants between 9.47–12.45%. These valuable physical features showed a ultrahigh specific capacitance of 401 $F g^{-1}$ and 235 $F g^{-1}$ in a two-electrode configuration system, using electrolytes of 1 M H_2SO_4 and 6 M KOH, respectively. Also, electrochemical properties were evaluated in the form of pellet binder-free materials. Porous carbon sources were known to generate extensive specific energy of 55.69 $Wh kg^{-1}$ and specific power of 200.09 $W kg^{-1}$. Based on the technique and results, the use of hierarchical 3D-porous carbon derivatives is validated as robust electrode materials in developing high-performance electrochemical energy storage.

Introduction

Excessive fossil fuel consumption rates are allegedly responsible for the persistent global energy crisis, high cost of alternative sources, and low efficiency in renewable energy conversion. This phenomenon has also triggered massive development of more energy-efficient storage devices.[1] The use of batteries and supercapacitors are commonly combined to substitute the huge dependency on bio-sources, particularly in electric vehicles. In comparison, carbon-based supercapacitors appear uniquely valuable, in terms of superior reversibility, infinite life cycle (EDLC type), and extensive power density (500–10,000 $W kg^{-1}$).[1,2] Therefore, application prospects are possible across a wide range of high energy devices, including electric vehicles, smart power grids, and laser systems. However, complex preparation processes, extreme production costs, and low specific energy (1–10 $Wh kg^{-1}$) are major limiting factors.[2,3]

Most researches assume the modification and possible development of electrode material are critical in specific energy improvement. Porous carbon provides excellent and appropriate electrical conductivity, wettability, chemical, and thermal properties.[4] However, manipulating and converting the biomass to permeable carbon samples in the electrodes are valid instruments in reducing fabrication costs and simplifying the heteroatom-enriched preparation techniques responsible for EDLC pseudo-capacitance behaviors.[5,6] In addition, biomass-based materials offer an extensive surface area to serve as multiple ion active contact points at the electrode/electrolyte interface, resulting in an enriched electrical double-layer and greater specific energy.[7] Furthermore, carbon's unique characteristics permit versatility, compared to other elements, and also enable immediate bonding with surrounding atoms, using various hybridizations. This condition generates allotropes with completely separate properties as well as confirms the potential application of porous carbon biomass in high-energy supercapacitor electrodes. Previous investigations have also recorded several biomass species as precursors to porous carbon materials, including tea waste,[8] grape marcs,[9] Juncus effuses,[10] and jengkol shell.[11] *Moringa Olifiera*-based activated carbon produced a high surface area of 2,250 $m^2 g^{-1}$ and specific energy of 25.8 $Wh kg^{-1}$, approximately three times the earlier report.[12] Meanwhile, mangosteen exhibited almost similar electrochemical properties with a surface area up to 2,300 $m^2 g^{-1}$.[13] Recent studies revealed the high electrode performance was not barely influenced by extensive surface area, but was also due to the presence of micro, meso, and macro pore structures (hierarchical), in expanding energy and power rates.[14] Furthermore, micro-pores consistently provide a large surface area ranging between 2,000–3,000 $m^2 g^{-1}$, with only 1/3 accessibility to electrolyte ions.[15,16] This circumstance demonstrates a significant impact on degraded ion mobility at high currents and also tends to reduce the specific power, although mesopores and macropores are needed to shorten the migration pathways. A suitable combination of these three pore types shows a tendency to properly conserve substantial power while increasing the specific energy.

Recently, biomass-based hierarchical porous carbon exhibited superior electrochemical properties, using various methods and are synthesized with a hard or salt template strategy,[17,18] metal organic framework,[19,20] physical activation, chemical activation, or in combined applications.[21,22] These techniques remarkably yielded a micro/meso/macropores ratio suitable for high specific energy and power sustainability. Previous report

[a] Prof. Dr. E. Taer, A. Apriwandi
Department of Physics, Faculty of Mathematic and Natural Science
University of Riau
Jl. Kampus Binawidya Km. 12.5, Panam, Pekanbaru (Indonesia)
E-mail: erman.taer@lecturer.unri.ac.id

[b] Dr. R. Taslim
Department of Industrial Engineering
State Islamic University of Sultan Syarif Kasim, Riau
Jl. H.R. Soebrantas Km. 15, Simpang Baru-Tampan, Pekanbaru (Indonesia)

by Wu et al. (2020) showed hierarchical porous carbon was obtained from wood tar precursors, by the template technique, where specific energy up to 33.87 Wh kg^{-1} was generated.[23] On the other hand, Wei et al., (2019) acquired similar results with the use of leaf samples, through physical activation and KOH impregnation.[24] Apart from the ability to form high surface area and pore size distribution in suitable ratio for relatively large conductive carbon materials, most synthetic methods appear very complex. This is due to the inclusion of time-consuming templates with strict reactions, metal frameworks capable of severe environmental damage, and physical/chemical activation, where dominant micro-pores were obtained. Therefore, it is very important to develop an effective strategy in generating hierarchical pore structures with suitable pore size distribution and high heteroatom content.

The effective performance of supercapacitors is further enhanced by the synergistic heteroatom effects, including nitrogen, oxygen, boron, phosphorus, and sulfur.[25,26] In porous carbon, electrode capacity is improved by the electrolyte's wettability behavior. As a consequence, pseudo-capacitive properties are formed, although with reduced electrode resistance. Furthermore, the effect of heteroatoms on biomass precursors has attracted wide attention in the development of electrochemical energy storage devices.[26,27] Biomass wastes, particularly plant residues, have been considered as excellent alternatives due to large volume of organic content.[28] Among the various compost, dried banana leaf biomass offers a promising precursor as a result of oxygen, carbon, hydrogen, nitrogen, potassium, magnesium and sulfur in rich volumes.[29,30] A simple technique to synthesize porous carbon doped heteroatom, based on biomass involves chemical activation at high temperature during pyrolysis, specifically KOH impregnation.[16,31] This process tends to reduce the heteroatom, particularly N and O.[32,33] Furthermore, $ZnCl_2$ activating reagent is considered successful in preserving the natural morphology of the 3D structures.[34,35] However, no report of using dried banana leaf samples for this exact investigation has been recorded. Furthermore, KOH and $ZnCl_2$ impregnated is a technique that is often used to obtain porous carbon-based on biomass.[36] This impregnation can more effectively decompose complex compounds of lignocellulosic biomass, including hemicellulose, cellulose, and lignin to produce high pure carbon. KOH impregnation degrades complex compounds into small molecules, resulting in a relatively high specific surface area.[37,38] However, excessive degradation due to strong activation of KOH removes most of the carbon atoms, resulting in very low pure carbon fixed. Moreover, $ZnCl_2$ impregnation is considered a relatively mild salt-based chemical activating agent and is effective in producing high porosity carbon.[39] In addition, $ZnCl_2$ is effective in generating heteroatoms as self-doping agents that could improve the electrochemical performance of carbon electrodes for supercapacitor application.[34]

The applied technique in this study appears relatively simple, time-saving and does not involve template/metal framework/metal oxide. In addition, the precursors are directly converted to heteroatom doped self-hierarchical porous activated carbon by chemical/physical activation ($ZnCl_2$/CO_2) in the form of binder-free pellets. The results showed the use of $ZnCl_2$ and CO_2 resulted in 3D hierarchical pore morphology with high oxygen levels in the range of 9.47–12.45%. Moreover, the specific surface area was increased from 429.590 to 860.410 m^2 g^{-1} with a clear micro/meso/macro-pore size distribution, while the symmetric supercapacitor was evaluated in two aqueous electrolytes of 1 M H_2SO_4 and 6 M KOH with the best performance demonstrating excellent electrochemical properties, including high capacitance 401 F g^{-1}, specific energy 55.69 Wh kg^{-1}, and specific power 200.09 W kg^{-1}.

Results and Discussion

3.1. Physical properties analyses

Figure 1(a) shows the density of porous carbon-based materials, due to $ZnCl_2$ impregnation and direct pyrolysis in the presence of N_2/CO_2. The densities of BL700, ABL700, ABL800, and ABL900 samples prior to pyrolysis were specified at 1.0100, 0.9700, 0.9800, and 0.9700 g cm^{-3}, respectively, with a mean standard deviation of 0.0627. Previous reports confirmed these values within the specifications for activated carbon binder-free sources. However, the variables declined drastically after the process by 0.8280, 0.6500, 0.5400, and 0.6200 g cm^{-3}, correspondingly, with a mean standard deviation of 0.0662.

The results were believed to validate the $ZnCl_2$ impregnation in very high temperature pyrolysis responsible for the water content reduction, volatilities, and the breakdown of complex carbon compounds. Furthermore, $ZnCl_2$ served as a dehydrating agent to disintegrate the H and O chains in the functional groups fewer than 700 °C.[34] This resulted in a decreased density from BL700 to ABL700 by approximately 32.8%. However, the $ZnCl_2$ is assumed very effective at temperatures below 500 °C, and in subsequent reaction with carbon, hydrated zinc chloride ($ZnCl_2$·nH_2O) was formed.[39,40] Increasing heat effect tends to hydrolyze $ZnCl_2$·nH_2O and produce oxychloride. Also, an upsurge in the physical activation temperature from 700–800 °C significantly declined the density by 44.6%, as confirmed in ABL800. The addition of a higher pyrolysis temperature influences porosity, and triggers the opening of new pores, enlarges narrow pores, as well as expands the existing pore sizes, causing a maximum reduction in ABL800 by 44.6%. Interestingly, ABL900 showed a slightly greater density after pyrolysis, compared to ABL800, due to carbon pore extension. Consequently, the pore walls appeared incapable of sustaining the new opening, leading to the collapse of the pore structure, and the occurrence of slightly higher density in ABL900, compared to ABL800.

The crystal structure of banana leaves-based porous carbon was evaluated using X-ray diffraction (XRD) technique. Figure 1(b) reveals two broad-bands in the XRD profile at $2\theta = 23$–$25°$ and 43–45° (JCPDS: 00-041-1487), respectively correlated with 002 and 100 reflection planes similar to graphite-like carbonaceous structures. Also, BL700 observed two broad-bands at $2\theta = 25.99°$ (002) and $2\theta = 44.56°$ (100), accompanied by several sharp peaks. Apart from unordered carbon arrange-

ments, various element/compound crystal structures, including K atom at $2\theta = 35°$ and $2\theta = 37°$,[41] $CaO/CaCO_3$ at $2\theta = 29°$, and $2\theta = 32°$, as well as SiO_2 at $2\theta = 39°$ and $2\theta = 42°$ (JCPDS 89-1668, 82-1690), were discovered. These occurrences tend to increase the internal resistance in porous carbon materials and inhibit the electrical properties of supercapacitor electrodes. Furthermore, $ZnCl_2$ inclusion at various temperature range between 700–900 °C in ABL700, ABL800, and ABL900 generated slightly separate profiles from the precursor type with two broad-bands, particularly in the 002 reflection plane towards the smaller unit of $2\theta = 23°$. This circumstance was due to extensive pyrolysis temperature assumed to disrupt the graphite carbon arrangement and form random shifts in adjacent layers, resulting in a turbo-static carbon structure.[42,43] The above mentioned characteristics are useful in enriching carbon pores. In addition, higher heat application from 700–800 °C in ABL700 and ABL800 samples reduced sharp peaks in the XRD profiles, as well as K, $CaO/CaCO_3$, and SiO_2 elements/compounds in carbonaceous substances. These results certainly considered suitable electrical properties for porous carbon electrodes. However, extreme temperatures up to 900 °C is assumed to enhance the degree of pseudo-crystallinity, despite the distance from the graphite crystallinity orientation.[44] This tends to return the sharp peaks at low intensity, as confirmed in AL900. Table 1 represents the $ZnCl_2$ impregnated samples from 700–900 °C with accompanying changes in interlayer spacing (d_{002}, d_{100}) and pseudo-crystalline dimensions (L_c, L_a). The d_{002}/d_{100} values within the range of 3.415–3.693 Å/2.032–2.127 Å were observed to be higher, compared to graphite-based materials.[43,45] This suggested the formation of amorphous carbon structures, with closely similar values, as reported in several previous studies. In observing the physical properties of the carbon-based derivatives for high-performance supercapacitors, pseudo-crystalline dimension of L_c/L_a is often associated with specific surface area, based on several earlier reports.[46] The high surface area is confirmed by a relatively larger L_c/L_a ratio. Table 1 shows the ABL800 sample with the highest L_c/L_a ratio, and predicts the possibility of maximum specific surface area. This result corresponded to the characterization of N_2 adsorption/desorption isotherm.

SEM techniques with several magnifications were applied to evaluate the morphological structure of $ZnCl_2$ activated banana leaves-derived carbon at various pyrolysis temperatures. The samples possessed a lignocellulose complex component comprising cellulose, hemicellulose, and lignin polymers. $ZnCl_2$ impregnated component served as a dehydration/dehydrogenation agent to eliminate the complex matrix bonds between lignocellulose elements, in order to form a fully dislocated porous carbon framework. Figure 2(a) describes these processes to simultaneously generate pore combinations within certain sizes, as confirmed in the surface morphology of ABL700 sample. In addition, ABL700 SEM micrographs observed the presence of macro-pores in the range of 54–392 nm, where the enlargement was marked with a white portion. Also, minor amount of meso-pores occurred between the estimates of 27–38 nm, but with a relatively flat/smooth surface. During pyrolysis at 700 °C, zinc chloride reacted directly with the entire carbon matrix. Oxychloride was formed as a by-product at low

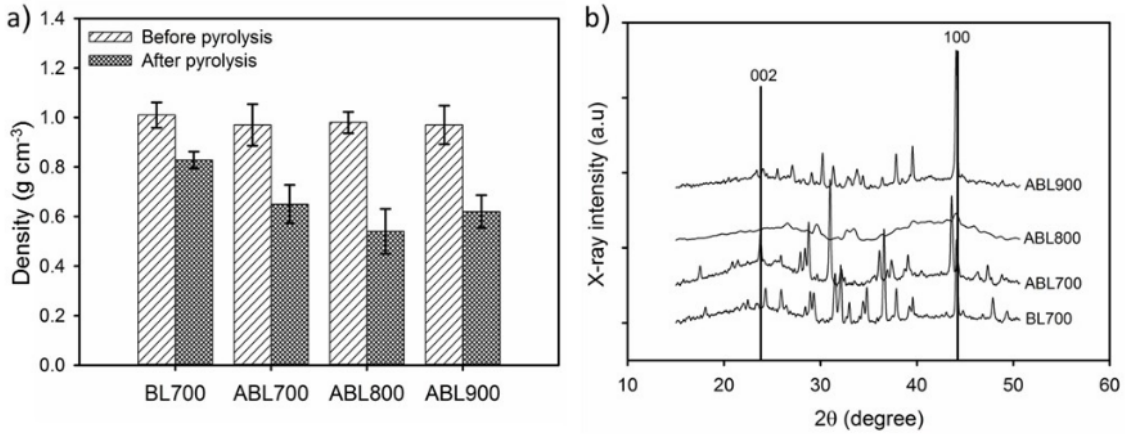

Figure 1. (a) Density of carbon coin solids free-binder before and after pyrolysis; (b) The XRD pattern of porous carbon derived banana leaves.

Table 1. The average spacing between layers/d_{002},d_{100} and the pseudo-crystalline dimensions/L_c,L_a of porous carbon derived banana leaves.

Samples	$2\theta_{002}$ [°]	$2\theta_{100}$ [°]	d_{002} [Å]	d_{100} [Å]	L_c [Å]	L_a [Å]	L_c/L_a
BL700	25.232	44.111	3.509	2.073	9.263	37.478	0.247
ABL700	25.112	42.508	3.415	2.127	7.972	30.644	0.260
ABL800	24.077	43.616	3.693	2.032	6.401	21.752	0.294
ABL900	24.885	42.612	3.575	2.120	7.152	26.962	0.265

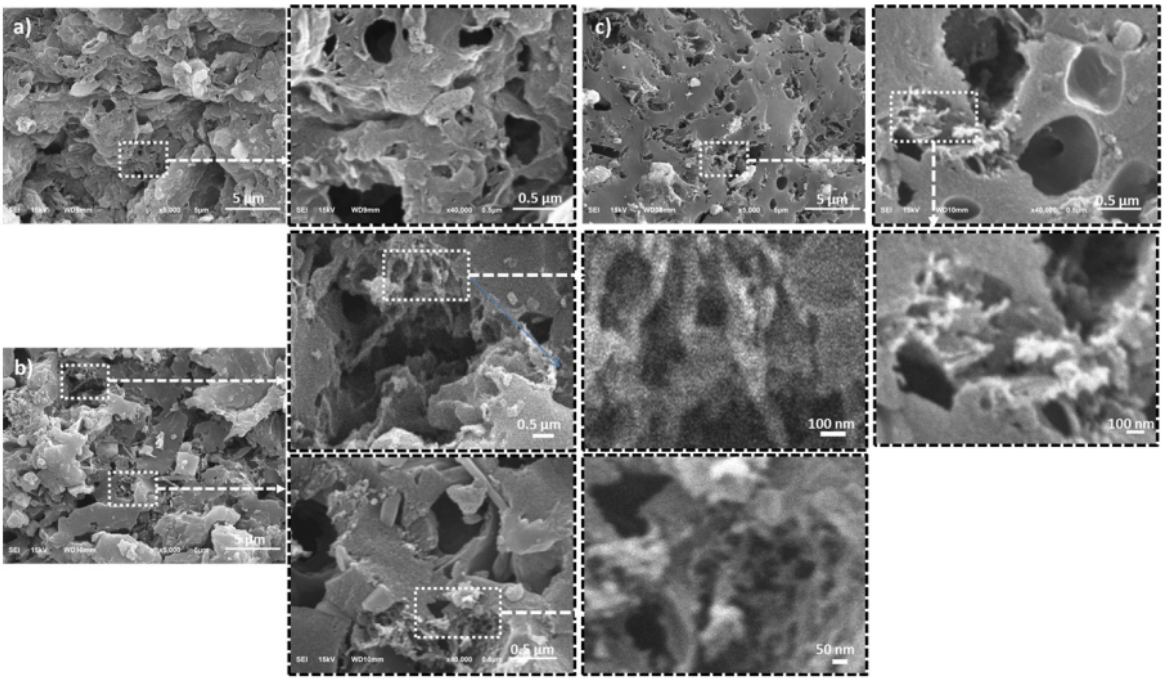

Figure 2. SEM image for (a) ABL700; (b) ABL800; (c) ABL900.

temperatures, as the inert gas was discharged, leaving behind a porous carbon framework interspersed with zinc oxide.[47] In addition, increasing the heat to 800 °C simultaneously evaporated zinc oxide and other impurities.[40] This situation unexpectedly confirmed the combination of hierarchically linked macropores and mesopores, as represented on ABL800 SEM micrograph (Figure 2(b)), with various magnifications. The resulting macro-pores and mesopores varied in sizes within the range of 57–288 nm and 14–27 nm, respectively. Under higher intensity, the ABL800 samples validated the presence of the 3D macro/mesopores, with uniform surface distribution. In addition, high-temperature pyrolysis in a CO_2 gas allows for carbon purification with an active surface. These characteristics are indispensable, in terms of enhancing high electrode performance in renewable energy storage systems.[48,49] Consequently, the morphological structure was maintained as a stable macro/meso 3D pores structure without obvious collapse (Figure 2(c)), after carbonization and high temperature re-arrangement at 600 °C and 900 °C, respectively. However, both macro-pore and meso-pore sizes shifted towards a larger range between 101–773 nm and 36–46 nm, correspondingly. These configurations provided high ionic active contact and structural stability in support of extensive functionality in energy storage systems.[50]

The surface functional groups instigated an intense ion migration on the electrode layer, as $ZnCl_2$ impregnation at high pyrolysis temperatures tends to result in additional polar groups on biomass-based activated carbon materials. Figure 3 shows FTIR technique was most suitable in evaluating these components, and also generates the spectrum of porous carbon-banana leaves, based on BL700, ABL700, ABL800, and ABL900 samples. In general, the entire raw materials were pyrolyzed at high temperatures, in order to reduce absorption p[79]s. Furthermore, the optimal absorbance of about 3612–3596 cm^{-1} and 1503–1477 cm^{-1} matched the stretching vibrations of –OH and C–OH hydroxyl groups, respectively.[51] Obviously, ABL800 and AL900 demonstrated a robust absorbance, compared to BL700 and ABL700, as a result of high temperature $ZnCl_2$

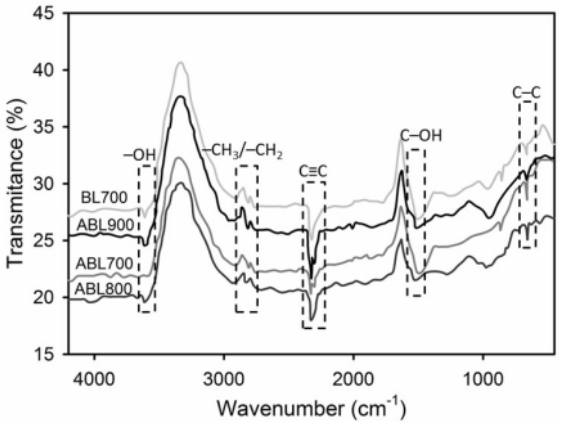

Figure 3. FTIR spectrum for BL700, ABL700, ABL800, and ABL900.

impregnation >800 °C. However, C–OH was dominated by ABL700, while high absorbance of –OH strain possibly influenced the device's pseudo-capacitive properties. The peak of $-CH_3$/$-CH_2$ at wave number of 2828–2751 cm^{-1} was clearly diminished with increasing pyrolysis temperature, due to incomplete carbonization and activation, where butyl ester was substituted with hydroxyl group.[52] The chemical reaction of $ZnCl_2$ with precursor carbon at high-temperature pyrolysis can hydrolyze $ZnCl_2{\cdot}nH_2O$ and produce oxychloride (ZnOCl). Increasing the pyrolysis temperature from 700 °C to 900 °C allows the production of more ZnOCl due to their interaction with CO_2 gas. Evaporation of Zn due to high temperature can etch the carbon matrix chains thereby initiating the formation of a 3D pore structure, as confirmed by SEM micrograph. Rich-free oxygen is left behind to bind to the activated carbon in the matrix. Thus, the sample is significantly affected by the heteroatom effect, as confirmed in FTIR spectrum (–OH and C–OH hydroxyl groups). In addition, the functional groups of CC, and C–C occurred at the peak of 2330 cm^{-1} and 702 cm^{-1}, and strongly confirmed the $ZnCl_2$ impregnated samples at high temperature, as the entire materials were dominated with high carbon content.[53] This analysis is also relevant to the EDS characterization further discussed.

The EDS analysis was aimed at corroborating individual element content of the banana leaf samples. In addition, the spectrum observed the location of two initial peaks at 0.277 and 0.525 eV, where abundant carbon with oxygen were confirmed (Figure 4). However, BL700 indicated a relatively high number of spectrum peaks with a dominant carbon of 57.59%, followed by other impurities, including calcium, oxygen, silica, and potassium compositions of 18.98, 17.50, 4.60, and 1.33%, with energy peaks of 3.690, 0.525, 1.739, and 3.312 eV, respectively. The $ZnCl_2$ impregnation at various pyrolysis temperatures tends to influence the carbon concentrations and other elements in the ABL samples. Under activation temperature of 700 °C, the carbon drastically inclined by 70.09% and oxygen by 20.54%, while calcium, silica, and potassium showed a gradual reduction (Figure 4(b)), due to possible oxidization of the precursor material and decrease in basic biomass elements.[54,55] Increasing the physical activation temperature to 800 and 900 °C in ABL800 and ABL900, respectively, tends to greatly improve the carbon spectrum between 82.54–82.79%, (Figure 4(c, d)). Moreover, spectrum peaks of the impurities, including oxygen, silica, and potassium observed a corresponding decline by 12.45–9.47%, 5.36–3.22%, 1.79–1.73%, and 0.76–0.00%. The high carbon percentage in ABLs provided a relatively large amount of active contact area by boosting the electrode performance.[56,57] Additionally, oxygen, as the second-highest element, contributes in a different way. $ZnCl_2$ impregnation at high temperatures of 700 °C to 900 °C significantly enriches elemental oxygen. This is due to the formation of high oxychloride compounds accompanied by evaporation of Zn due to high temperatures, which results in high oxygen contributed to oxide compounds. The carbon precursor will also benefit from increased wettability as well as surface hydrophilicity and pseudo-capacitive properties.[58,59] This circumstance was also confirmed in the cyclic voltammetry and galvanostatic charge discharge analyses. Therefore, the wett-

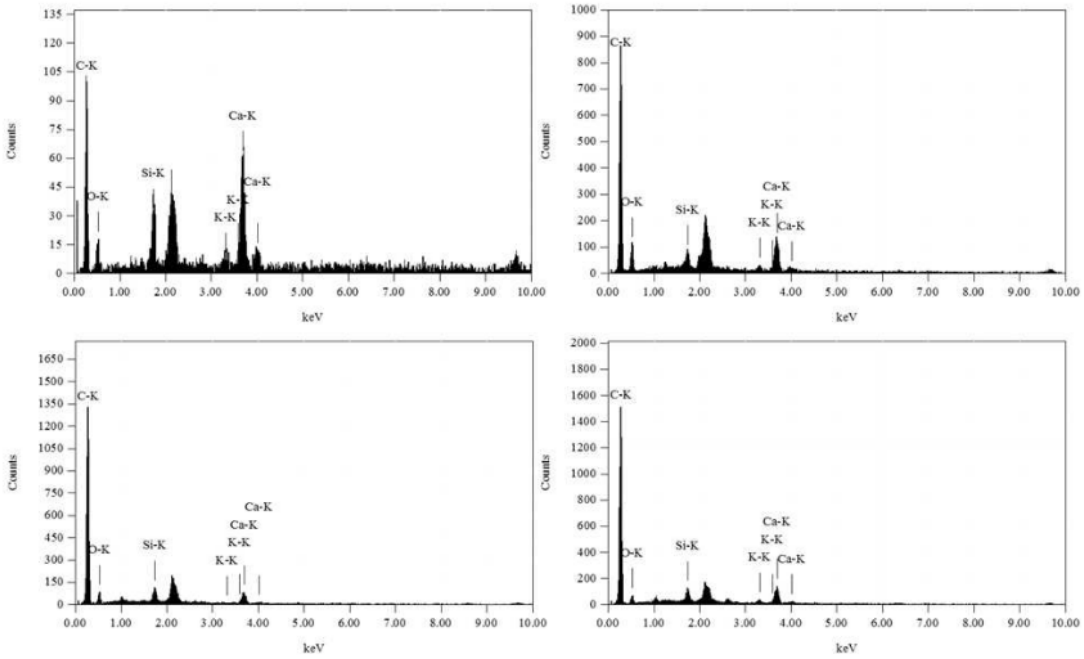

Figure 4. EDS spectrum for (a) BL700; (b) ABL700; (c) ABL800; and (d) ABL900.

ability and hydrophilic behavior of the electrode surface also contributed significantly in promoting the electrostatic adsorption of supercapacitors.

The porosity behavior, surface area, and various pore size structures are described as the major characteristics in evaluating the potential of hierarchical porous activated carbon potential. Also, N_2 gas adsorption/desorption provides a precise/accurate method for determining specific surface area and pore size distribution. Figure 5 shows the N_2 adsorption/desorption isotherm associated with IV type is typical for the complete samples.[60] However, BL700 generated a steadily low linear absorption at relative pressure $P/P0 < 0.4$, followed by loop hysteresis at $0.4 < P/P0 < 0.95$. This assumed a consistent occurrence of micro-and mesopores with relatively low pore volume of 0.4322 $cm^3 g^{-1}$ and specific surface area of 429.590 $m^2 g^{-1}$. Interestingly, hysteresis loop formation was not completely closed due to developing mesopores structure in bottle cap shape, with a narrow neck cavity for imperfect capillary condensation.[3] During $ZnCl_2$ injection at separate high temperatures, the entirely prepared porous carbon sources exhibited an ideal combination of type IV characteristics and H4 hysteresis loops, as observed in ABL700, ABL800, and ABL900 profiles. The close proximity of horizontal adsorption-desorption lines varying at $P/P0 < 0.35$, indicated relatively extensive micro-pores and an entirely locked hysteresis loop at $0.45 < P/P0 < 0.95$, with a random normal mesopores structure in the carbon matrix.[61] Furthermore, adsorption spike at $0.95 < P/P0 < 1.0$ revealed the presence of minor macropores.[14] This validated the formation of hierarchically connected micro/meso/macro-pore structures during the impregnation. Subsequently, the carbon element reacted with zinc chloride at $< 600\,^{\circ}C$ in the presence of an inert gas to produce zinc oxychloride. Subsequently, at high pyrolysis temperature $< 800\,^{\circ}C$, the zinc oxide decomposed to form micro/mesopores.[62,63] This leads to increase the specific surface area by 860.410 $m^2 g^{-1}$ with total volume of 0.8974 $cm^3 g^{-1}$. Higher activation temperature $> 900\,^{\circ}C$ evaporated the element/compound of Zn/CO_2 as an impurity, causing a pore size expansion and the existence of hierarchically linked 3D meso/macropores. These results confirmed the previously reported SEM images. In addition, the pore size extension showed a decline in specific surface area to 626.844 $m^2 g^{-1}$, with a total volume of 0.6436 $cm^3 g^{-1}$. Figure 6 represents the pore size distribution, using BJH method. The entire samples acknowledged the presence of micro, meso, and macropores responsible for the hierarchical 3D pore structure.

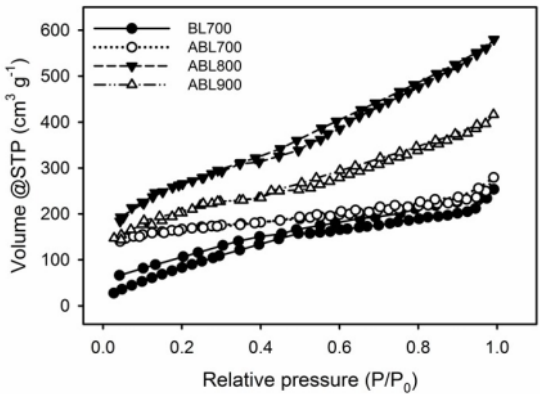

Figure 5. N_2 adsorption/desorption isotherm profile of BL700, ABL700, ABL800, and ABL900.

Consequently, the pore size distribution clearly demonstrated sub-micro-pores with an increased absorption volume, and is described as a very important characteristic in the reduction of δ value, using capacitance equation. In addition, the presence of varying mesopores triggered the uniform migration of electrolyte ions, without major resistance.[55,64] Lesser amounts of macroporosity provided an all-directional ion transport pathway. The $ZnCl_2$ Impregnation at similar pyrolysis temperature (700 °C) tends to increase the micro-pore absorption volume from 0.1344 to 0.158 $cm^3 g^{-1}$, with possible reduction in the average pore diameter of 3.34 nm, as represented in Table 2. In addition, the higher pyrolysis temperatures drastically boosted the presence of micro- and mesopores as well as the absorption volume, followed by an improvement in mesoporosity by 44%, based on ABL800. These characteristics are useful in reducing the electrode cell resistance.[65,66] Also, higher temperatures slightly lowered the average pore diameter to 4.10 nm, as confirmed in ABL900. Table 2 represents the porosity properties of the samples.

3.2. Electrochemical behavior analyses

The electrochemical characteristics of banana leaves-based supercapacitor electrodes were evaluated using cyclic voltammetry and galvanostatic charge-discharge methods with 1 M H_2SO_4 and 6 M KOH aqueous electrolytes. Figure 7(a) shows the CV profiles scanned at 1 $mV s^{-1}$, using 1 M H_2SO_4 solution. The profiles resembled a typical distorted rectangular-like shape accompanied by an angled hump over a potential ranges. This

Table 2. The porosity properties of banana leaves-based porous carbon materials.

Samples	S_{BET} [$m^2 g^{-1}$]	S_{micro} [$m^2 g^{-1}$]	S_{meso} [$m^2 g^{-1}$]	V_{tot} [$cm^3 g^{-1}$]	V_{micro} [$cm^3 g^{-1}$]	V_{meso} [$cm^3 g^{-1}$]	D_{aver} [nm]	Mesoporosity [%]
AC700	429.590	222.013	207.577	0.4323	0.1330	0.253	4.52	48
ACZ700	516.963	300.51	216.402	0.4864	0.1580	0.2742	3.34	41
ACZ800	860.410	480.163	380.163	0.8974	0.2994	0.598	4.17	44
ACZ900	626.844	339.259	287.585	0.6436	0.2096	0.434	4.10	45

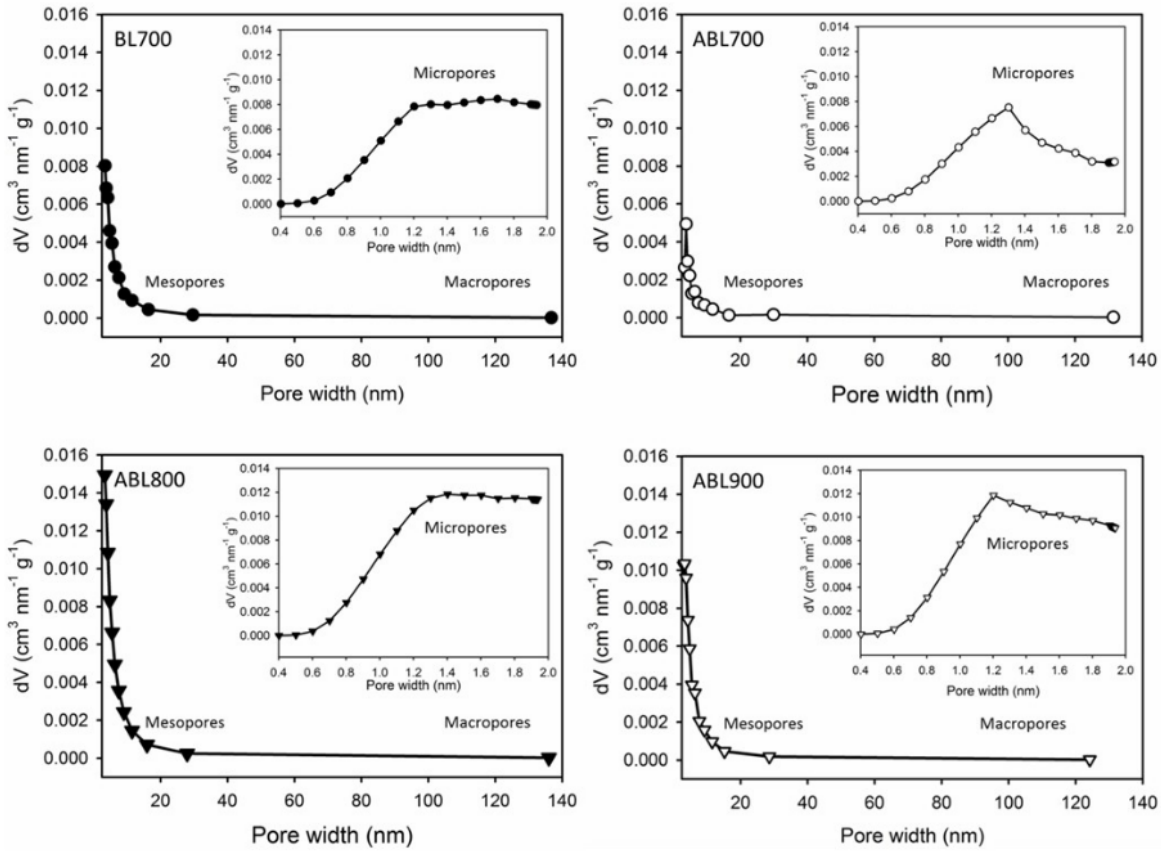

Figure 6. Pore size distribution of BL700, ABL700, ABL800, and ABL900.

confirms the common electrochemical double-layer (EDLC) properties, followed by a redox reaction as pseudo-capacitance behavior was derived from self O-heteroatom doping.[67,68] Furthermore, the precursor type observed the most regular rectangular shape, compared to others. However, the resulting specific capacitance was relatively lesser, and was specified at 56 $F g^{-1}$, with a specific energy of 8.05 $Wh kg^{-1}$. The typical high-temperature pyrolysis of $ZnCl_2$-activated samples at ABL700, ABL-800, and ABL-900 generated potential indentation humps within the range of 0.2–0.8 V. This suggested the mutual behavior of EDLC and pseudo-capacitive properties was due to self-oxygen heteroatom dopants.[69] In addition, higher carbon content, superior specific surface area, and the presence of hierarchically connected pores were known to significantly extend the capacitive properties by 238, 365, and 219 $F g^{-1}$ in ABL700, ABL800, and ABL900, respectively. Figure 7(a) confirms the increase in oxygen in ABL700 clearly showed an improved pseudo-capacitive properties and specific energy by 33.05 $Wh kg^{-1}$. These increments also instigated further development of 3D hierarchical micro/meso-rich pores and maximum capacitance while sustaining the pseudo-capacitive behavior. The scattered pores are beneficial to the electrolyte ions towards generating additional electrostatic layers, providing diffusion space in every directions,[70] maintaining a relatively short diffusion distance to obtain high capacitive properties of 365 $F g^{-1}$ as well as boosting the specific energy and power to 49.44 $Wh kg^{-1}$ and 178.18 $W kg^{-1}$, respectively. However, an extension in pyrolysis temperature above 900 °C is expected to reduce the O-heteroatom, while retaining ABL900 pseudo-capacitance features. In addition, the presence of various macropores also exhibited superior capacitive with specific energy and specific power estimated at 30.41 $Wh kg^{-1}$ and 109.61 $W kg^{-1}$, respectively.

Figure 7(b) shows the change in specific capacitance with a higher scan rate of 10 $mV s^{-1}$. Each sample activated by $ZnCl_2$ during pyrolysis was believed to maintain relatively extensive capacitive properties in the range of 60–80%. However, BL700 demonstrated a reasonably large reduction in specific capacitance at 45.3%. The ABL800 samples reported the maximum capacitive property of 308 $F g^{-1}$ and maintained 84.2% specific capacitance at a scan rate of 10 $mV s^{-1}$. The presence of 3D hierarchical pores and O-heteroatom doping effects was proved

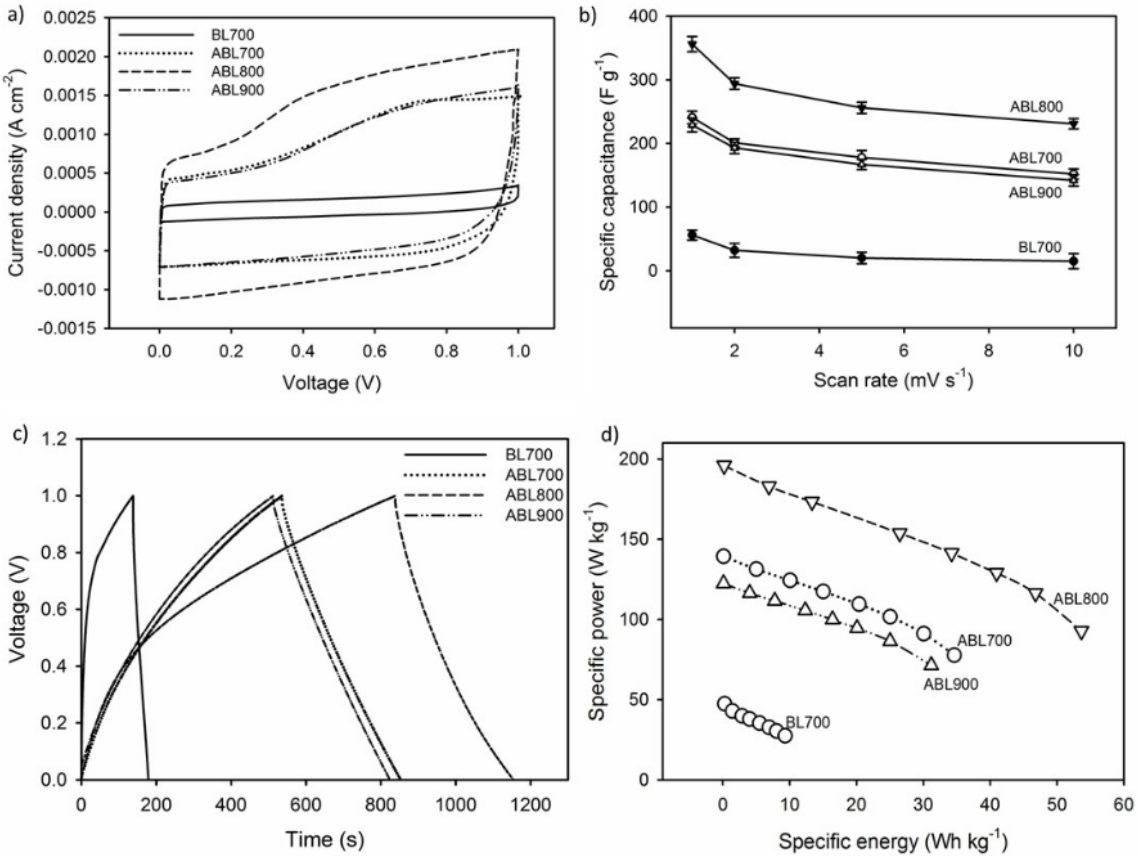

Figure 7. (a) CV profile for all samples; (b) Csp vs. scan rate curve; (c) GCD profiles for all samples in 1 M H2SO4 electrolyte; and (d) Ragone plot in 1 M H_2SO_4 electrolyte.

effective in sustaining the ion transfer and formation of a double electricity layer on the electrode material. Furthermore, ABL700 and ABL900 showed specific capacitances of 175 and 154 Fg^{-1} while conserving 73.5% and 70.32%, respectively, at a scan rate of 10 mVs^{-1}.

Figure 7(c) represents the GCD technique used to evaluate the symmetric supercapacitor with the 1 M H_2SO_4 electrolyte. This profile described a quasi-triangular shape, denoting a combination of EDLC and pseudo-capacitive properties. Table 3 observed a relative iR drop. The BL700 generated a considerably lesser GCD profile with a specific capacitance of 61 Fg^{-1}. Furthermore, $ZnCl_2$ injection at 700 °C unexpectedly enhanced the capacitive properties of the cell to 258 Fg^{-1}. This contributed to a high specific surface area with a suitable pore combination responsible for improved electrode performance. However, the ABL800 showed higher charge and discharge

Table 3. The electrochemical performance of the electrode supercapacitor based on self-oxygen-doped 3D porous carbon derived banana leaves waste.

Samples	CV technique						GCD technique							
	1 M H_2SO_4			6 M KOH			1 M H_2SO_4				6 M KOH			
	C_{sp} [Fg^{-1}]	E_{sp} [$Whkg^{-1}$]	P_{sp} [Wkg^{-1}]	C_{sp} [Fg^{-1}]	E_{sp} [$Whkg^{-1}$]	P_{sp} [Wkg^{-1}]	C_{sp} [Fg^{-1}]	E_{sp} [$Whkg^{-1}$]	P_{sp} [Wkg^{-1}]	R [mΩ]	C_{sp} [Fg^{-1}]	E_{sp} [$Whkg^{-1}$]	P_{sp} [Wkg^{-1}]	R [mΩ]
BL700	56	8.05	29.03	31	2.92	10.51	61	9.16	33.09	8	–	–	–	–
ABL700	238	33.05	119.12	124	17.22	62.06	258	35.83	129.25	22	198	27.50	99.19	41
ABL800	365	49.44	178.18	179	24.86	89.58	401	55.69	200.90	10	235	32.63	117.62	35
ABL900	219	30.41	109.61	119	16.53	59.55	241	33.47	120.74	9	181	25.14	90.68	12

time duration, compared to other samples with the highest specific capacitance of 401 $F g^{-1}$. The blend of hierarchically connected micro/meso/macropores, high surface area with large mesoporosity of 44%, and contribution of self O-heteroatom doping was believed to successfully increase the specific capacitance by 401 $F g^{-1}$ and the specific energy up to 55.69 $Wh kg^{-1}$ with a specific power of 200.09 $W kg^{-1}$. This specific energy obtained was relatively 5 times above the range in Reagon's plot.[63] Furthermore, higher temperature of 900 °C exhibited a partial triangular profile with proven common and EDLC/pseudo-capacitive properties, despite the reduced oxygen content. The specific capacitance in ABL900 sample was estimated at 241 $F g^{-1}$ with specific energy and specific power of 33.47 $Wh kg^{-1}$ and 120.74 $W kg^{-1}$, respectively. In comparison, the electrochemical properties showed an improved performance, compared to several previous studies (Table 4). In addition, Figure 7(d) performed the Ragone plot of BL700, ABL700, ABL-800, and ABL-900 samples. As shown in Figure 7(d), the highest specific energy was found as high as 55.69 $Wh kg^{-1}$ at optimum specific power of 200.90 $W kg^{-1}$ at ABL800 sample.

Figure 8(a) highlights the evaluation of supercapacitor cells in a 6 M KOH electrolyte for a two-electrode system, aimed at providing a comprehensive analysis on capacitive properties. The CV curve was in the form of a distorted rectangular shape, indicating the normal features of the electric double layer. In addition, self- oxygen heteroatom effect was confirmed, but not very clearly. Specific capacitances for BL700, ABL700, ABL800, and ABL900 were generated at 31, 124, 179, and 119 $F g^{-1}$, respectively. Figure 8(b) consistently shows a quasi-triangular shape enhancing the normal EDCL properties, followed by a pseudo-capacitive in 6 M KOH alkaline electrolyte. Based on the GCD profile, the specific capacitances of BL700, ABL700, ABL800, and ABL900 were estimated at 46, 198, 235, and 181 $F g^{-1}$, correspondingly. These values were relatively lesser, compared to the 1 M H_2SO_4 acid electrolyte. Generally, acid and alkaline electrolytes are known to influence electrochemical properties by the anionic and cationic sizes, mobility, as well as the conductivity depending on the pore size distribution of the base materials. In this study, cationic H^+ obtained a smaller ionic size than K^+, with the ability to penetrate very minor pores and extend to the overall electrode openings. Conversely, K^+ with a relatively larger ionic size tends to reduce ionic mobility and the electrode's specific capacitance.[71] In addition, H^+ cation with optimal ionic conductivity of 350.1 $cm^2 \Omega^{-1} mol^{-1}$, represented almost five times the K^+ cation of 73.5 $cm^2 \Omega^{-1} mol^{-1}$, and therefore, are allowed to migrate more easily towards the electrode/electrolyte interface.[72] Furthermore, the GCD profile of the 6 M KOH electrolyte clearly indicated a relative iR drop. The ABL700 sample produced a cell resistance of 41 mΩ, while higher pyrolysis temperatures on ABL800 and ABL900 tend to lower the cell resistance to 35 and 12 mΩ, respectively. This variation was caused by the increasing pore structure and the mesoporosity presented at the electrodes. Also, $ZnCl_2$ and physical activation temperature increment possibly extended the pore size distribution, in a bid to promote smooth ion accessibility at the electrode/electrolyte interface, without any form of resistance. Moreover, the overall samples were also scanned at a higher speed of 10 $mV s^{-1}$ in a 6 M KOH electrolyte to maintain the device's capacity between 50–70%. In addition, ABL800 demonstrated the maximum retention of 69.98% (Figure 8(c)), and was also able to produce optimal capacitive properties in the 6 M KOH electrolyte. This confirmed the presence of 3D hierarchical pores and self-oxygen heteroatom dopant with the tendency to enhance the electrochemical properties of super-

Table 4. Materials and electrochemical properties of heteroatom doped porous carbons compared to different sources in symmetrical supercapacitor.

Sources	Electrode type	Dopant	Pores structure	S_{BET} [$m^2 g^{-1}$]	Electrolyte	C_{sp} [$F g^{-1}$]	E_{sp} [$Wh kg^{-1}$]	P_{sp} [$W kg^{-1}$]	Refs.
Microcrystalline cellulose	Carbon aerogel	–	Interconnected pores	646	6 M KOH	160	17.81	180.11	[77]
Wild jujube pit	AC-powder	O (6.7%)	Interconnected micro-, meso-, macropores	2438	1 M Na_2SO_4	260	13.33	16,000	[78]
Indicalamus leaves	AC-powder	–	3D Hierarchical porous	1801	6 M KOH	326	23.70	224.5	[79]
Soybean meal	AC-powder	N (6.84%), O (12.6%), P (1.53%)	Interconnected Honeycomb structure	483	1 M H_2SO_4	360	10.00	–	[31]
Pollen-cone	AC-powder	–	Hierarchical porous	2314	ILGPE	146	21	190	[36]
Fir bark	Carbon composite	N (20%), B (13%)	Sphere-like	955	6 M KOH	91	9.33	400	[80]
Peanut shell	AC-powder	N (2.8%)	Hierarchical porous	2014.6	6 M KOH	306	40.92	990	[81]
Urine	AC-powder	N (7.8%), O (7.4%), S (0.8%)	Hierarchical porous	1040.5	6 M KOH	166	12.7	337.84	[82]
Quinone-amine polymer	AC-powder	N (14.9%), O (10.6%)	Nano-sphere	2957.8	6 M KOH	273.9	8.0	–	[83]
Pomelo peels	AC-powder	O (11.00%)	Hierarchical porous	1194	6 M KOH	144	–	–	[84]
Chinese fir wood sawdust	AC-powder	O (6.79), N (0.47)	Hierarchical porous	2361	6 M KOH	324	–	–	[85]
Banana leaves	AC-pellets	O (12.45%)	3D porous	860.410	1 M H_2SO_4	401	55.69	200.90	This work

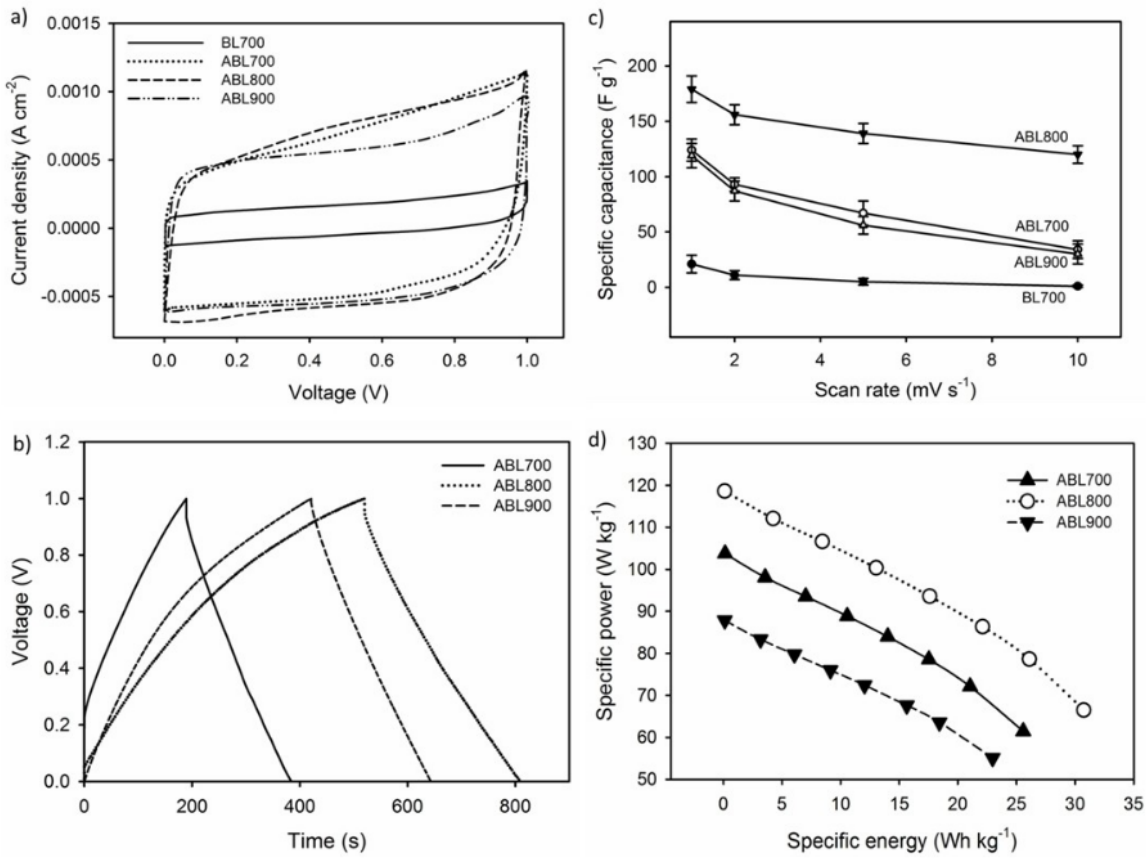

Figure 8. (a) CV profile for all samples; (b) Csp vs. scan rate curve; (c) GCD profiles for all samples in 6 M KOH electrolyte (d) Ragone plot in 6 M KOH electrolyte.

capacitor electrodes. In addition, the specific energy and specific power also evaluated in 6 M KOH electrolyte, as shown in Figure 8(d). Ragone plot in Figure 8(d) confirmed that The ABL800 sample has highest specific energy of 32.63 Wh kg^{-1} at optimum specific power of 117.62 W kg^{-1}.

Generally, various techniques are employed in measuring electrochemical properties, including CV and GCD. However, the selected methods are not expected to exhibit conflicting results. In this research, the two above mentioned procedures were employed to demonstrate the respective contributions, in terms of evaluating the performance of electrochemical properties, particularly in a two-electrode configuration system. Furthermore, the CV approach utilized current density data, based on a fixed voltage window at a specified scan rate, while GCD indicated the time data measured against a voltage with a constant current density.[73] The cumulative results confirmed the properties of the sample supercapacitor. This study, however, revealed a slight variation in capacitive properties between CV and GCD. The specific capacitance generated by GCD demonstrated fairly higher value, compared to CV, due to considerable complex parameters of GCD.[74] Moreover, GCD measurement possibly validated the voltage drop, internal resistance, and reactance, in order to acquire abundant specific capacitance between 5–10%, compared to CV.[75,76] These outcomes are in accordance with the provisions outlined in Table 3. Overall, the analysis was also presented by several researchers with experience in the application of the two applied techniques.

Conclusion

A self-oxygen doped 3D porous carbon material was prepared by a combination of chemical and physical activations using $ZnCl_2$ and CO_2. Dried banana leaves as precursors were purely synthesized to 3D-porous activated carbon with the aid of a free-template/free-metal framework. The various physical activation temperatures tend to increase the specific surface area from 429.590 to 860.410 m^{2}g^{-1}, with mesoporosity levels occurring between 41–52%. Furthermore, $ZnCl_2$ activated

samples at 800 °C showed the best physical properties with maximum surface area of 860,410 m^2 g^{-1}, carbon content 82.54%, high oxygen heteroatom dopant 12.54%, and valid amorphous properties. The electrochemical characteristics were evaluated in the form of pellets with binder-free materials, using 1 M H_2SO_4 electrolyte. Subsequently, an excellent performance with 365 $F g^{-1}$ capacitive properties at a scan rate of 1 $mV s^{-1}$ was achieved, alongside the sustainability potential of 84.2% at a scan rate of 10 $mV s^{-1}$. The 3D porous carbon demonstrated optimal specific capacitance in ABL800 at 401 $F g^{-1}$ and a constant current density of 1 $A g^{-1}$, with specific energy and specific power of 55.69 $Wh kg^{-1}$ and 200.09 $W kg^{-1}$, respectively. In addition, the electrochemical properties were also determined, using 6 M KOH alkaline electrolyte with a specific capacitance of 235 $F g^{-1}$ and current density of 1.0 $A g^{-1}$, with maintenance capacitive of 70% at a scan rate of 10 $mV s^{-1}$. However, the high meso-porosity level of the samples proved the existence of low cell resistance within the range of 9–41 mΩ. These favorable results indicated the possibility of self-oxygen heteroatom 3D porous carbon components from dried banana leaves to produce excellent electrochemical behavior in supercapacitors.

Experimental Section

Synthesis of self O-heteroatom doping porous carbon

Dried banana leaves were acquired from Riau, Indonesia, while $ZnCl_2$ and H_2SO_4 were purchased from Marck KGaA, CAS-No: 764–857 and Panreac Quimica S.A.U, 131058, 1612, respectively. The synthesis of O-heteroatom self-doping porous carbon commenced with the initial waste treatment, involving washing, evaporation, and pre-carbonization. First, the precursors were cut into minor portions, 1×2 cm, and rinsed with de-ionized (DI) water, subsequently evaporated and oven-dried for two days at 110 °C, followed by pre-carbonization at 250 °C. The resulting materials were pulverized, using milling tools and 53 micron sieve. A total of 0.5 m/L of $ZnCl_2$ was added to 30 g of pre-carbonized powder in 150 mL water solvent. Furthermore, the powder/$ZnCl_2$ mixture was placed on the hot plate at 300 rpm under a temperature of 80 °C for two hours. This stage was proceed with precipitation and further drying to obtain a chemically activated powder sample, as well as the conversion into solid coins, using hydraulic press with binder-free materials. Solid coins were known to undergo direct pyrolysis by single step carbonization and physical activation in a horizontal furnace tube. The carbonization process was initialized between 30–600 °C in an N_2 gas environment at a heat rate of 3 °C/min, followed by physical activation involving three separate high temperatures at 700, 800, and 900 °C in a CO_2 gas environment with flow rate of 10 ml/min. Lastly, the resulting materials were neutralized using DI water. However, in an effort to facilitate accurate data analysis, these samples were labeled on the basis of varying pyrolysis temperatures, including BL700 at 700 °C without $ZnCl_2$ impregnation. Meanwhile, ABL700, ABL800, and ABL900 impregnated samples were observed at 700, 800, and 900 °C, respectively. In detail, preparation 3D porous carbon from self-oxygen doped biomass-based for supercapacitor was shown in Scheme 1.

Material Characterizations

Solid coin binder-free materials were initially evaluated using mass, thickness and diameter in density reduction. The crystal properties were measured by x-ray diffraction with the use of Philip Expert 2.1 instrument with Cu radiation (λ = 0.154 nm) in the range of 10–60° on a 2θ scale. Average spacing between layers/d_{002},d_{100} and pseudo-crystalline dimensions/L_c,L_a were determined by Bragg's law and Scherer equation, respectively. In addition, the surface functional group was assessed by Fourier-Transform Infrared Spectroscopy (FTIR) at Shimadzu, and IR Prestige-21 instrument with wave range of 4500–450 cm^{-1}. Furthermore, JEOL JSM-6510(LA) was utilized to observe the surface morphology and element status at a voltage of 15 kV in the energy range of 0–20 keV. Nitrogen adsorption/desorption was also estimated using the Quantachrome-NOVA 1200, while the specific surface area and the pore size distribution were calculated by Brunauer-Emmet-Teller (BET) and Barret-Joiner-Halenda (BJH) methods, respectively.

Electrochemical measurement

The measurement of electrochemical properties, including cyclic voltammetry (CV) and galvanostatic charge discharge (GCD) was achieved, using a handmade instrument CV/CD-UR Rad-Er 5841/2018, with calibrated error, ±6.0%. In addition, the CV method involved a 0.0–1.0 V potential window with several scan rates covering 1, 2, 5 and 10 $mV s^{-1}$, while GCD was conducted at a

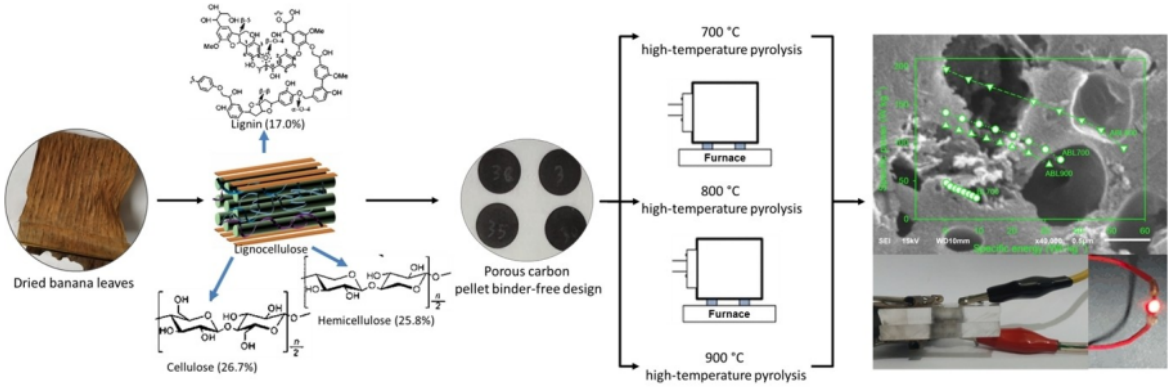

Scheme 1. Preparation 3D porous carbon from Self-Oxygen Doped Biomass-Based for supercapacitor.

constant current of 1 A, with a scan rate of 1 $mV s^{-1}$. Supercapacitor cells were arranged in a two-electrode system of 9 mm diameter. However, the BL/ABLs active materials were placed on a 3×3 cm acrylic body cells, with an organic separator between the electrodes and aqueous electrolyte, composed of 1 M H_2SO_4 and 6 M KOH. The specific capacitance was calculated from CV process using the equation:[86]

$$C_{sp} = \Delta I/s \cdot m \quad (1)$$

Where C_{sp} refers to the specific capacitance ($F g^{-1}$), ΔI is the difference between the charge and the discharge currents (A), s is the scan rate ($mV s^{-1}$), and m is the working electrode mass. Based on the GCD technique, the specific capacitance was evaluated using the equation:[53,87]

$$C_{sp} = I \cdot \Delta t/m \cdot \Delta V \quad (2)$$

Where C_{sp} refers to the specific capacitance ($F g^{-1}$), I is the constant current (A), Δt is the discharge time (s), m is the working electrode mass (g), and ΔV is the change in discharge voltage (V). Moreover, specific energy and specific power were also calculated using the equations:[53,87]

$$E_{sp} = C_{sp} \cdot V^2/7.2 \quad (3)$$

$$Psp = 3600 \cdot E_{sp}/\Delta t \quad (4)$$

Where E_{sp} is the specific energy ($Wh kg^{-1}$), C_{sp} is the specific capacitance ($F g^{-1}$), V is the voltage (V), where the voltage window is used in CV and the discharge voltage for GCD, P_{sp} is the specific power ($W kg^{-1}$), and Δt is the discharge time (s).

Acknowledgements

The research was financially supported by first year Project of Word Class Research (WCR) in Kementerian Pendidikan, Kebudayaan, Riset, dan Teknologi, Republic of Indonesia (contract no. 1393/UN.9.1.5/PT.01.03/2021) with the title "High energy and power dens of supercapacitor for the optimization of electrode supply process".

Conflict of Interest

The authors declare no conflict of interest.

References

Keywords: heteroatom doping · porous carbon · hierarchical porous · electrode materials · supercapacitor

[1] agaki, H. Konno, O. Tanaike, *J. Power Sources* **2010**, *195*, 7880–7903.
[2] Poonam, K. Sharma, A. Arora, S. K. Tripathi, *J. Energy Storage* **2019**, *21*, 825.
[3] R. T. Ayinla, J. O. Dennis, H. M. Zaid, Y. K. Sanusi, F. Usman, L. L. Adebayo, aner Prod. **2019**, *229*, 1427–1442.
[4] Y. Zhai, Y. Dou, D. Zhao, P. F. Fulvio, R. T. Mayes, S. Dai, *Adv. Mater.* **2011**, *23*, 4828–4850.
[5] B. Wang, L. Ji, Y. Yu, N. Wang, J. Wang, J. Zhao, *Electrochim. Acta* **2019**, *309*, 34–43.
[6] S. Rangabhashiyam, P. Balasubramanian, *Ind. Crops Prod.* **2019**, *128*, 405–423.
[7] . Iqbal, S. Zakar, S. S. Haider, *J. Electroanal. Chem.* **2020**, *858*, 113793.
[8] T. Ratnaji, L. J. Kennedy, *Diamond Relat. Mater.* **2020**, *110*, 108100.
[9] J. Zhang, H. Chen, J. Bai, M. Xu, C. Luo, L. Yang, L. Bai, D. Wei, W. Wang, Yang, *J. Alloys Compd.* **2021**, *854*, 157207.
[10] Y. Ping, J. Han, J. Li, B. Xiong, P. Fang, C. He, *Diamond Relat. Mater.* **2019**, *100*, 107577.
[11] E. Taer, Apriwandi, R. Taslim, Agustino, *Mater. Today: Proc.* **2021**, DOI 10.1016/j.matpr.2020.11.644.
[12] alisoc, J. M. Dungo, M. Natividad, *Heliyon* **2020**, *6*, e03202.
[13] V. Yang, R. A. Senthil, J. Pan, A. Khan, S. Osman, L. Wang, W. Jiang, Y. n, *J. Electroanal. Chem.* **2019**, *19*, 113616.
[14] Y. Zhang, S. Yu, G. Lou, Y. Shen, H. Chen, Z. Shen, S. Zhao, J. Zhang, S. , Q. Zou, *J. Mater. Sci.* **2017**, *52*, 11201–11228.
[15] u, J. Chen, B. Cui, P. Yin, C. Zhang, *J. Carbon Res.* **2018**, *4*, 53.
[16] Q. Abbas, R. Raza, I. Shabbir, A. G. Olabi, *J. Sci. Adv. Mater. Devices* **2019**, 1–352.
[17] A. Xie, J. Dai, Y. Chen, N. Liu, W. Ge, P. Ma, R. Zhang, Z. Zhou, S. Tian, C. t al., *Adv. Powder Technol.* **2019**, *30*, 170–179.
[18] hen, D. Yu, X. Zheng, X. Dong, *J. Energy Storage* **2019**, *21*, 105–112.
[19] Y. P. Zhao, R. X. Xu, J. P. Cao, X. Y. Zhang, J. S. Zhu, X. Y. Wei, *J.* roanal. Chem. **2020**, *871*, 114288.
[20] D. Chu, F. Li, X. Song, H. Ma, L. Tan, H. Pang, X. Wang, D. Guo, B. Xiao, *J.* id Interface Sci. **2020**, *568*, 130–138.
[21] W. Jiang, J. Pan, Liu, *J. Power Sources* **2019**, *409*, 13–23.
[22] u, S. Li, J. Yang, J. Hu, *J. Colloid Interface Sci.* **2018**, *513*, 448–454.
[23] J. wu, M. Xia, X. Zhang, Y. Chen, F. Sun, X. Wang, H. Yang, H. Chen, *J.* er Sources **2020**, *455*, 227982.
[24] ei, J. S. Wei, Y. Li, H. Zou, *J. Power Sources* **2019**, *414*, 13–23.
[25] D. A. Hapidin, M. M. Munir, Suprijadi, K. Khairurrijal, *Aerosol Sci. Technol.* **2020**, *54*, 203–216.
[26] A. Gopalakrishnan, S. Badhulika, *J. Power Sources* **2020**, *480*, 228830.
[27] Y. Liu, Z. Chang, L. Yao, S. Yan, J. Lin, J. Chen, J. Lian, H. Lin, S. Han, *J. Electroanal. Chem.* **2019**, *847*, 113111.
[28] J. Yang, Y. Wang, J. Luo, L. Chen, *Ind. Crops Prod.* **2018**, *121*, 226–235.
[29] N. Sellin, D. Ricardo, C. Marangoni, O. Souza, *Renewable Energy* **2016**, *96*, -64.
[30] C. K. Roy, S. S. Shah, A. H. Reaz, S. Sultana, A. N. Chowdhury, S. H. Firoz, M. H. Zahir, M. A. Ahmed Qasem, M. A. Aziz, *Chem. Asian J.* **2021**, *16*, 296–308.
[31] Z. Guo, X. Kong, X. Wu, W. Xing, J. Zhou, Y. Zhao, S. Zhuo, *Electrochim.* **2020**, *360*, 137022.
[32] Y. Ma, X. Zhang, Z. Liang, C. Wang, Y. Sui, *Electrochim. Acta* **2020**, *337*, 135800.
[33] L. Zhang, G. Li, C. Dong, L. Jing, Z. Li, Z. Li, *Diamond Relat. Mater.* **2020**, 107691.
[34] H. Chen, H. Wei, N. Fu, W. Qian, Y. Liu, H. Lin, S. Han, *J. Mater. Sci.* **2018**, *53*, 2669–2684.
[35] C. Wang, T. Liu, *J. Alloys Compd.* **2017**, *696*, 42–50.
[36] A. A. Hor, S. A. Hashmi, *Electrochim. Acta* **2020**, *356*, 136826.
[37] L. Suárez, T. A. Centeno, *J. Power Sources* **2020**, *448*, 227413.
[38] M. Xu, Q. Huang, J. Lu, J. Niu, *Ind. Crops Prod.* **2021**, *161*, 113215.
[39] un, T. Jiang, G. Zhao, J. Shi, *Int. J. Electrochem. Sci.* **2019**, *14*, 1–14.
[40] P. González-García, *Renewable Sustainable Energy Rev.* **2018**, *82*, 1393–
[41] Y. Xi, D. Yang, X. Qiu, H. Wang, J. Huang, Q. Li, *Ind. Crops Prod.* **2018**, , 747–754.
[42] A. Yaya, B. Agyei-Tuffour, D. Dodoo-Arhin, E. Nyankson, E. Annan, D. S. Konadu, E. Sinayobye, E. A. Baryeh, C. P. Ewels, *Glob. J. Eng. Des. Technol.* **2018**, *1*, 32–41.
[43] J. Serafin, M. Baca, M. Biegun, E. Mijowska, R. J. Kaleńczuk, J. Sreńscek-Nazzal, B. Michalkiewicz, *Appl. Surf. Sci.* **2019**, *497*, 143722.
[44] X. Su, S. Li, S. Jiang, Z. Peng, X. Guan, X. Zheng, *Adv. Powder Technol.* **2018**, *29*, 2097–2107.
[45] E. Taer, A. Apriwandi, R. Taslim, A. Agutino, D. A. Yusra, *J. Mater. Sci.* nol. **2020**, *9*, 13332–13340.
[46] M. Deraman, R. Daik, S. Soltaninejad, N. S. M. Nor, Awitdrus, R. Farma, N. F. Mamat, N. H. Basri, M. A. R. Othman, *Adv. Mater. Res.* **2015**, *1108*, 1–
[47] X. Liu, C. Ma, J. Li, B. Zielinska, R. J. Kalenczuk, X. Chen, P. K. Chu, T. , E. Mijowska, *J. Power Sources* **2019**, *412*, 1–9.
[48] M. Yu, Y. Han, J. Li, L. Wang, *Chem. Eng. J.* **2017**, *317*, 493–502.

[49] E. Taer, A. Apriwandi, Y. Yusriwandi, W. S. Mustika, Z. Zulkifli, R. Taslim, S. Sugianto, B. Kurniasih, A. Agustino, P. Dewi, *AIP Conf. Proc.* **2018**, *1927*, 030036-1–030036-6.
[50] ang, M. Qiao, X. Mamat, *Appl. Surf. Sci.* **2021**, *540*, 148352.
[51] Y. Chen, Y. Jiang, Z. Liu, L. Yang, Q. Du, K. Zhuo, *Electrochim. Acta* **2021**, DOI 10.1016/j.electacta.2020.137414.
[52] Y. Liang, Y. Lu, G. Xiao, J. Zhang, H. Chi, Y. Dong, *Appl. Surf. Sci.* **2020**, *529*, 147141.
[53] Z. Dai, P. Ren, W. He, X. Hou, F. Ren, Q. Zhang, *Renewable Energy* **2020**, 613–623.
[54] A. M. Abioye, F. N. Ani, *Renewable Sustainable Energy Rev.* **2015**, *52*, 1282–1293.
[55] E. Taer, Apriwandi, B. K. L. Dalimunthe, R. Taslim, *J. Chem. Technol. Biotechnol.* **2021**, *96*, DOI 10.1002/jctb.6579.
[56] S. E. M. Pourhosseini, O. Norouzi, H. R. Naderi, *Biomass Bioenergy* **2017**, 287–298.
[57] R. Taslim, T. R. Dewi, E. Taer, A. Apriwandi, A. Agustino, R. N. Setiadi, *J. Phys. Conf. Ser.* **2018**, *1120*, 012084.
[58] K. Wang, N. Zhao, S. Lei, R. Yan, X. Tian, J. Wang, Y. Song, D. Xu, Q. Guo, L. Liu, *Electrochim. Acta* **2015**, *166*, 1–11.
[59] S. Liu, Y. Zhao, B. Zhang, H. Xia, J. Zhou, W. Xie, H. Li, *J. Power Sources* **2018**, *381*, 116–126.
[60] K. S. W. Sing, *Pure Appl. Chem.* **1982**, *54*, 2201–2218.
[61] A. H. Jawad, M. Bardhan, M. A. Islam, M. A. Islam, S. S. A. Syed-Hassan, S. N. Surip, Z. A. ALOthman, M. R. Khan, *Surfaces and Interfaces* **2020**, *21*, 100688.
[62] V. S. Bhat, P. Kanagavalli, G. Sriram, R. P. B., N. S. John, M. Veerapandian, urkuri, G. Hegde, *J. Energy Storage* **2020**, *32*, 101829.
[63] A. González, E. Goikolea, J. A. Barrena, R. Mysyk, *Renewable Sustainable Energy Rev.* **2016**, *58*, 1189–1206.
[64] T. R. Kumar, R. A. Senthil, Z. Pan, J. Pan, Y. Sun, *J. Energy Storage* **2020**, *32*, 101903.
[65] B. Chang, Y. Wang, K. Pei, S. Yang, X. Dong, *RSC Adv.* **2014**, *4*, 40546–2.
[66] A. Elmouwahidi, E. Bailón-García, A. F. Pérez-Cadenas, F. J. Maldonado-Hódar, F. C co-Marín, *Electrochim. Acta* **2017**, *229*, 219–228.
[67] H. Yang, J. Zhou, M. Wang, S. Wu, W. Yang, H. Wang, *Int. J. Energy Res.* **0**, *44*, 4449–4463.
[68] A. Pina, A. Amaya, J. Marcuzzo, A. Rodrigues, M. Baldan, N. Tancredi, A. Cuña, *J. Carbon Res.* **2018**, *4*, 24.
[69] Y. Guo, T. Wang, D. Wu, Y. Tan, *Electrochim. Acta* **2021**, *366*, 137404.
[70] S. Yang, S. Wang, X. Liu, L. Li, *Carbon* **2019**, *147*, 540–549.
[71] D. Momodu, N. Fatou, B. Mutuma, A. Bello, *J. Electroanal. Chem.* **2019**, 119–128.
[72] B. Pal, S. Yang, S. Ramesh, V. Thangadurai, R. Jose, *Nanoscale Adv.* **2019**, *1*, 3807–3835.
[73] C. Lämmel, M. Schneider, M. Weiser, A. Michaelis, *Materwiss. Werksttech.* **3**, *44*, 641–649.
[74] A. Balducci, D. Belanger, T. Brousse, J. W. Long, W. Sugimoto, *J. rochem. Soc.* **2017**, *164*, A1487–A1488.
[75] M. D. Stoller, R. S. Ruoff, *Energy Environ. Sci.* **2010**, *3*, 1294–1301.
[76] u, Y. Cai, S. Wang, Z. Li, *Int. J. Hydrogen Energy* **2021**, *46*, 2432–2444.
[77] X. Tian, S. Zhu, J. Peng, Y. Zuo, G. Wang, X. Guo, N. Zhao, Y. Ma, L. Ma, *Electrochim. Acta* **2017**, *241*, 170–178.
[78] K. Sun, S. Yu, Z. Hu, Z. Li, G. Lei, Q. Xiao, Y. Ding, *Electrochim. Acta* **2017**, 417–428.
[79] J. Huang, L. Chen, H. Dong, Y. Zeng, H. Hu, M. Zheng, Y. Liu, Y. Xiao, Y. Liang, *Electrochim. Acta* **2017**, *258*, 504–511.
[80] L. Luo, Y. Zhou, W. Yan, X. Wu, S. Wang, W. Zhao, *Electrochim. Acta* **2020**, *360*, DOI 10.1016/j.electacta.2020.137010.
[81] X. Jiang, F. Guo, X. Jia, Y. Zhan, H. Zhou, L. Qian, *J. Energy Storage* **2020**, 101451.
[82] F. Razmjooei, K. Singh, T. H. Kang, N. Chaudhari, J. Yuan, J. S. Yu, *Sci. Rep.* **2017**, *7*, 1–14.
[83] L. Zheng, X. Dai, Y. Ouyang, Y. Chen, X. Wang, *J. Energy Storage* **2021**, 02152.
[84] J. Han, Y. Ping, J. Li, Z. Liu, B. Xiong, P. Fang, C. He, *Diamond Relat. Mater.* **2019**, *96*, 176–181.
[85] S. Cao, J. Yang, J. Li, K. Shi, X. Li, *Diamond Relat. Mater.* **2019**, *96*, 118–
[86] V. Climent, J. M. Feliu, in *Encycl. Interfacial Chem. Surf. Sci. Electrochem.*, 3, pp. 48–74.
[87] D. K. Kampouris, X. Ji, E. P. Randviir, C. E. Banks, *RSC Adv.* **2015**, *5*, 12782–12791.

Manuscript received: September 28, 2021
Revised manuscript received: November 12, 2021
Accepted manuscript online: November 15, 2021
Version of record online: November 26, 2021

Ultrahigh Capacitive Supercapacitor Derived from Self-Oxygen Doped Biomass-Based 3D Porous Carbon Sources

ORIGINALITY REPORT

14%	9%	8%	4%
SIMILARITY INDEX	INTERNET SOURCES	PUBLICATIONS	STUDENT PAPERS

PRIMARY SOURCES

1	www.jstage.jst.go.jp Internet Source	<1%
2	D. W. Li, Y. S. Zhou, X. Huang, L. Jiang, J.-F. Silvain, Y. F. Lu. "In situ imaging and control of layer-by-layer femtosecond laser thinning of graphene", Nanoscale, 2015 Publication	<1%
3	Kovo G. Akpomie, Jeanet Conradie. "Sequestration of thiazolyl blue tetrazolium bromide and bromophenol blue onto biochar derived from American sycamore leaves", International Journal of Environmental Analytical Chemistry, 2022 Publication	<1%
4	digital.library.adelaide.edu.au Internet Source	<1%
5	www.kfupm.edu.sa Internet Source	<1%
6	www.imrfjournals.com Internet Source	<1%

7	www.koreascience.or.kr Internet Source	<1 %
8	B.H. Poornima, T. Vijayakumar. "Hydrothermal synthesis of Boron- doped porous carbon from Azadirachta Indica wood for supercapacitor application", Inorganic Chemistry Communications, 2022 Publication	<1 %
9	www.jmrt.com.br Internet Source	<1 %
10	Jinlong Hu, Lingzhi Zhang. " Achieving F-doped porous hollow carbon nanospheres with ultrahigh pore volume a gas–solid interface reaction ", Journal of Materials Chemistry A, 2021 Publication	<1 %
11	Juan Du, Aibing Chen, Yue Zhang, Shuang Zong, Haixia Wu, Lei Liu. "PVP-assisted preparation of nitrogen doped mesoporous carbon materials for supercapacitors", Journal of Materials Science & Technology, 2020 Publication	<1 %
12	Katarzyna Morawa Eblagon, Anna Malaika, Manuel Fernando R. Pereira, José Luís Figueiredo. "Cutting the green waste. Structure -performance relationship in	<1 %

functionalised carbon xerogels for hydrolysis of cellobiose", ChemCatChem, 2018
Publication

13	Submitted to Sungkyunkwan University Student Paper	<1 %
14	Sungun Wi, Jungjin Park, Sangheon Lee, Joonhyeon Kang et al. "Synchrotron-based x-ray absorption spectroscopy for the electronic structure of Li x Mn 0.8 Fe 0.2 PO 4 mesocrystal in Li + batteries", Nano Energy, 2017 Publication	<1 %
15	Submitted to University of Lincoln Student Paper	<1 %
16	english.energy.hust.edu.cn Internet Source	<1 %
17	pubmed.ncbi.nlm.nih.gov Internet Source	<1 %
18	Submitted to Bogazici University Student Paper	<1 %
19	Lorena Alcaraz, Francisco J. Alguacil, Félix A. López. " Microporous adsorbent from winemaking waste for the recovery of Mn( ) in liquid solutions ", The Canadian Journal of Chemical Engineering, 2020 Publication	<1 %

20	www.chinchemlett.com.cn Internet Source	<1 %
21	www.sigma-not.pl Internet Source	<1 %
22	Rui Deng, Danlian Huang, Wenjing Xue, Lei Lei, Chengyun Zhou, Sha Chen, Xiaofeng Wen, Xigui Liu. "How does the microenvironment change during the stabilization of cadmium in exogenous remediation sediment?", Journal of Hazardous Materials, 2020 Publication	<1 %
23	abis-files.atauni.edu.tr Internet Source	<1 %
24	oa.tib.eu Internet Source	<1 %
25	szkoladoktorska.zut.edu.pl Internet Source	<1 %
26	xxtcl.sxicc.ac.cn Internet Source	<1 %
27	Jing Ding, Xiangyang Zhou, Qian Wang, Chucheng Luo, Juan Yang, Jingjing Tang. " N, S Co ‐ Doped Porous Carbon from Antibiotic Bacteria Residues Enables a High ‐ Performance FeF □ 0.33H O Cathode for Li ‐ Ion Batteries ", ChemElectroChem, 2020 Publication	<1 %

28	Submitted to Universitas Diponegoro Student Paper	<1 %
29	www.chemistry.unt.edu Internet Source	<1 %
30	www.cnrs-imn.fr Internet Source	<1 %
31	Muhammad Miftahul Munir, Martin Adrian, Muzakki Burhanuddin, Ferry Iskandar. "Fabrication and structure optimization of expanded polystyrene (EPS) waste fiber for high-performance air filtration", Powder Technology, 2022 Publication	<1 %
32	Submitted to Saint Johns University Student Paper	<1 %
33	fdk.uin-suska.ac.id Internet Source	<1 %
34	wrap.warwick.ac.uk Internet Source	<1 %
35	M Agustina, A Linggawati, K Arifin. " Cos as Co-Catalyst for Enhancing the Tio Photoelectrochemical Water Splitting ", Journal of Physics: Conference Series, 2019 Publication	<1 %
36	Yue Dai, Tangtong Ju, Hailong Tang, Meiling Wang, Min Wang, Yongqing Ma, Ganhong	<1 %

	Zheng. " N ‐ doped TiO ‐ quantum dots tightly anchored on graphene with superior interfacial contact via C–Ti bond ", Applied Organometallic Chemistry, 2021 Publication	
37	pub.iapchem.org Internet Source	<1 %
38	research-information.bris.ac.uk Internet Source	<1 %
39	yonghu.zjnu.edu.cn Internet Source	<1 %
40	Submitted to Birla Institute of Technology and Science Pilani Student Paper	<1 %
41	Hamidreza Parsimehr, Ali Ehsani. "Algae-based electrochemical energy storage devices", Green Chemistry, 2020 Publication	<1 %
42	Jinzhao Han, Yunjie Ping, Shiju Yang, Yuanming Zhang et al. "High specific power/energy, ultralong life supercapacitors enabled by cross-cutting bamboo-derived porous carbons", Diamond and Related Materials, 2020 Publication	<1 %
43	Submitted to Universidad de Alicante Student Paper	<1 %

44	bibliotekanauki.pl Internet Source	<1 %
45	carbon.buct.edu.cn Internet Source	<1 %
46	edepot.wur.nl Internet Source	<1 %
47	eprints.whiterose.ac.uk Internet Source	<1 %
48	fisika.fmipa.unri.ac.id Internet Source	<1 %
49	jglobal.jst.go.jp Internet Source	<1 %
50	www.sciopen.com Internet Source	<1 %
51	M. F. Y. M. Hanappi, M. Deraman, M. Suleman, M. A. R. Othman et al. "Preparation and characterization of graphene/turbostratic carbon derived from chitosan film for supercapacitor electrodes", AIP Publishing, 2018 Publication	<1 %
52	jcpr.kbs-lab.co.kr Internet Source	<1 %
53	Lijun Fu, Qunting Qu, Rudolf Holze, Veniamin V. Kondratiev, Yuping Wu. "Composites of	<1 %

metal oxides and intrinsically conducting polymers as supercapacitor electrode materials: the best of both worlds?", Journal of Materials Chemistry A, 2019
Publication

54	Submitted to Pondicherry University Student Paper	<1 %
55	cjas.agriculturejournals.cz Internet Source	<1 %
56	esst.cip.com.cn Internet Source	<1 %
57	Emanuela Calcio Gaudino, Giancarlo Cravotto, Maela Manzoli, Silvia Tabasso. " From waste biomass to chemicals and energy microwave-assisted processes ", Green Chemistry, 2019 Publication	<1 %
58	Submitted to University of Nottingham Student Paper	<1 %
59	Wentao Zhai, Bin Hu, Mengya Li, Junjie Jiang, Mengnan Zhou. "Dimensional Accuracy Control and Compressive Property of Microcellular Polyetherimide Honeycomb Foams Manufactured by an In Situ Foaming Fused Deposition Modeling Technology", Advanced Engineering Materials, 2021 Publication	<1 %

eprints.ncl.ac.uk

60	Internet Source	<1%
61	www.walshmedicalmedia.com Internet Source	<1%
62	Syed Shaheen Shah, Md. Almujaddade Alfasane, Idris Akolade Bakare, Md. Abdul Aziz, Zain H. Yamani. "Polyaniline and heteroatoms–enriched carbon derived from Pithophora polymorpha composite for high performance supercapacitor", Journal of Energy Storage, 2020 Publication	<1%
63	Tao, F.. "Electrochemical characterization on cobalt sulfide for electrochemical supercapacitors", Electrochemistry Communications, 200706 Publication	<1%
64	Submitted to University of Surrey Student Paper	<1%
65	refubium.fu-berlin.de Internet Source	<1%
66	Marceta Kaninski, M.P.. "Catalytic activity of Pt-based intermetallics for the hydrogen production-Influence of ionic activator", Applied Catalysis A, General, 20070329 Publication	<1%

67	Submitted to Universidade do Porto Student Paper	<1 %
68	Submitted to University of Adelaide Student Paper	<1 %
69	downloads.hindawi.com Internet Source	<1 %
70	www.nmletters.org Internet Source	<1 %
71	Abdulmajid A. Mirghni, Damilola Momodu, Kabir O. Oyedotun, Julien K. Dangbegnon, Ncholu Manyala. "Electrochemical analysis of Co 3 (PO 4) 2 ·4H 2 O/graphene foam composite for enhanced capacity and long cycle life hybrid asymmetric capacitors", Electrochimica Acta, 2018 Publication	<1 %
72	Arcila Henao Juan Sebastián. "Generación de gránulos y aglomerados microalga - bacteria para el tratamiento de aguas residuales municipales y producción de metano", TESIUNAM, 2017 Publication	<1 %
73	Hsieh, C.T.. "Fabrication and electric capacitive behavior of hetero-junction carbon nanoclusters by using secondary chemical	<1 %

vapor deposition", Chemical Physics Letters, 20070817
Publication

74	Lua, A.C.. "Preparation and characterization of activated carbons from oil-palm stones for gas-phase adsorption", Colloids and Surfaces A: Physicochemical and Engineering Aspects, 20010130 Publication	<1 %
75	S. B. Tang, M. O. Lai, L. Lu. " Characterization of crystallized LiMn O thin films grown by pulsed laser deposition ", Philosophical Magazine, 2007 Publication	<1 %
76	digibug.ugr.es Internet Source	<1 %
77	epub.uni-regensburg.de Internet Source	<1 %
78	publications.waset.org Internet Source	<1 %
79	www.elsevier.es Internet Source	<1 %
80	Ping Jiang, Lei Yan, Xicui Zhang, Hongyan Yuan, Dan Xiao, MartinâM.âF. Choi. "Electrogenerated Chemiluminescence Sensor Based on Tris(2,2â²-bipyridine)ruthenium(II)-	<1 %

Immobilized Natural Clay and Ionic Liquid", Electroanalysis, 2010

Publication

Exclude quotes	Off	Exclude matches	Off
Exclude bibliography	Off		